TOPICAL REVIEW — High pressure physics

A-site ordered quadruple perovskite oxides $AA'_3B_4O_{12}$*

Youwen Long(龙有文)[1,2,†]

[1] Beijing National Laboratory for Condensed Matter Physics, Institute of Physics, Chinese Academy of Sciences, Beijing 100190, China
[2] Collaborative Innovation Center of Quantum Matter, Beijing 100190, China

(Received 18 August 2015; revised manuscript received 30 September 2015; published online 30 May 2016)

The A-site ordered perovskite oxides with chemical formula $AA'_3B_4O_{12}$ display many intriguing physical properties due to the introduction of transition metals at both A' and B sites. Here, research on the recently discovered intermetallic charge transfer occurring between A'-site Cu and B-site Fe ions in $LaCu_3Fe_4O_{12}$ and its analogues is reviewed, along with work on the magnetoelectric multiferroicity observed in $LaMn_3Cr_4O_{12}$ with cubic perovskite structure. The Cu–Fe intermetallic charge transfer ($LaCu^{3+}_3Fe^{3+}_4O_{12} \rightarrow LaCu^{2+}_3Fe^{3.75+}_4O_{12}$) leads to a first-order isostructural phase transition accompanied by drastic variations in magnetism and electrical transport properties. The $LaMn_3Cr_4O_{12}$ is a novel spin-driven multiferroic system with strong magnetoelectric coupling effects. The compound is the first example of cubic perovskite multiferroics to be found. It opens up a new arena for studying unexpected multiferroic mechanisms.

Keywords: high-pressure synthesis, A-site ordered perovskite, charge transfer, multiferroicity

PACS: 81.40.Vw, 71.27.+a, 75.30.–m, 77.84.–s **DOI:** 10.1088/1674-1056/25/7/078108

1. Introduction

Transition-metal (TM) oxides with ABO_3 perovskite and/or perovskite-like structures have received much attention due to their varied crystal structures and their physical properties such as ferroelectricity, piezoelectricity, multiferroicity, superconductivity, colossal magnetoresistance, and catalysis.[1–12] As shown in Fig. 1(a), the B site in an ABO_3 perovskite oxide is usually occupied by a TM ion with BO_6 octahedral coordination, which dominates the electronic properties, while the A site often accommodates a relatively large cation such as an alkaline metal, alkaline-earth metal or rare earth element, located in the octahedral voids to sustain the structural framework. Since the crystal structure of perovskite is very flexible, one may prepare various structurally ordered perovskite oxides by appropriate chemical substitution. For instance, when a TM ion resides in the B site, a B-site ordered double perovskite $A_2BB'O_6$ can be formed (see Fig. 1(b)). One well-known example is the half-metallic ferrimagnetic compound Sr_2FeMoO_6 with a high Curie temperature (T_C) of about 420 K.[13] This relatively high T_C has stimulated considerable research on the family of 3d–4d and 3d–5d hybrid magnetic materials with high spin ordering temperatures. In particular, in the series of Cr-based double perovskites $Sr_2CrB'O_6$, the T_C increases from 458 K for $B' =$ W to 635 K for $B' =$ Re and further to 725 K for $B' =$ Os.[13–19] This trend in increasing T_C has been interpreted as a strong super-exchange interaction between fully occupied up-spin Cr-t_{2g} and Os-t_{2g} electrons.[16]

In addition to the B-site ordered double perovskites, so-called A-site ordered quadruple perovskites with chemical formula of $AA'_3B_4O_{12}$ also exist and can be obtained when three fourths of the A sites in a simple ABO_3 perovskite are occupied by TM ions A'.[20] This specially ordered perovskite usually crystallizes to a cubic lattice with space group Im-3 as shown in Fig. 1(c). Owing to the introduction of TM ions, which have smaller ionic radii, at the initially 12-fold-coordinated A site, the BO_6 octahedra are highly tilted in this ordered structure (A typical B–O–B bond angle is about 140°). As a result, high pressure is often necessary to prepare A-site ordered perovskites. Unlike BO_6 octahedral coordination, a transition metal at the A' site forms a square-planar-coordinated $A'O_4$ unit. As a result, some Jahn–Teller active ions like Cu^{2+} and Mn^{3+} can often occupy this site. Since both A' and B sites accommodate transition metals in A-site ordered quadruple perovskites, multiple magnetic and electrical interactions can take place through A'–A', B–B, and/or A'–B interaction pathways, giving rise to many interesting physical properties and potential applications. For example, ferromagnetism caused by the A'-site Cu^{2+} was found in the B-site nonmagnetic $CaCu_3B_4O_{12}$ ($B =$ Ge, Sn).[21] Colossal and temperature-independent dielectric constants ($\approx 10^5$) were observed in $CaCu_3Ti_4O_{12}$.[22,23] Large low-field magnetoresistance effects were shown in Ca/La/$BiCu_3Mn_4O_{12}$.[24–26] Magnetic and dielectric coupling occur in $BiMn_3Mn_4O_{12}$.[27] A recent study of $LaMn_3Ti_4O_{12}$ revealed that the A site can be occupied by Mn with an unusual low valence state rather than Jahn–Teller Mn^{3+}.[28] Some of these intriguing physical properties have already been reviewed in a few articles.[20,29]

*Project supported by the National Basic Research Program of China (Grant No. 2014CB921500), the Strategic Priority Research Program of the Chinese Academy of Sciences (Grant No. XDB07030300), and the National Natural Science Foundation of China (Grant No. 11574378).

†Corresponding author. E-mail: ywlong@iphy.ac.cn

© 2016 Chinese Physical Society and IOP Publishing Ltd

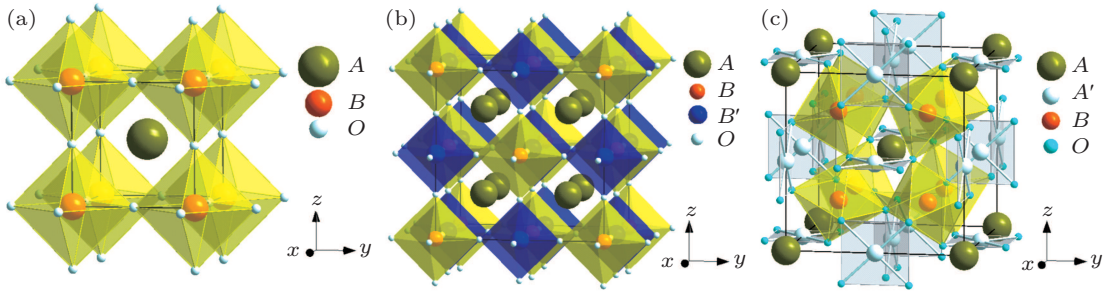


Fig. 1. (color online) (a) Crystal structure of simple perovskite ABO_3 with a Pm-3m space group. Atomic sites: A 1a (0, 0, 0), B 1b (0.5, 0.5, 0.5), O 3c (0, 0.5, 0.5); (b) crystal structure of B-site ordered double perovskite $A_2BB'O_6$ with an Fm-3m space group. Atomic sites: A 8c (0.25, 0.25, 0.25), B 4a (0, 0, 0), B' 4b (0.5, 0.5, 0.5), O 24e (x, 0, 0); (c) crystal structure of A-site ordered quadruple perovskite $AA'_3B_4O_{12}$ with an Im-3 space group. Atomic sites: A 2a (0, 0, 0), A' 6b (0, 0.5, 0.5), B 8c (0.25, 0.25, 0.25), O 24g (x, y, 0).

In the present invited review, we focus on the recent progress in A-site ordered quadruple perovskite oxides, including the intermetallic charge transfer between the A-site Cu and the B-site Fe in $ACu_3Fe_4O_{12}$ (A = La–Tb, and Bi), and magnetoelectric multiferroicity in the cubic perovskite-structure $LaMn_3Cr_4O_{12}$.[30–36]

2. Intermetallic charge transfer in $ACu_3Fe_4O_{12}$

Charge transfer occurring between two different transition metals can simultaneously change the valence states and electronic configurations of these two TM ions. It may lead to a series of related phase transitions in lattice, spin, charge and orbital degrees of freedom. Although intermetallic charge transfer is often observed in organic–inorganic hybridized systems,[37–40] only a few inorganic solid-state oxides show this phenomenon. Several A-site ordered perovskites $ACu_3Fe_4O_{12}$ (A = La–Tb, and Bi) were found to display intermetallic charge transfer between the A'-site Cu and the B-site Fe ions.[31–35]

The $ACu_3Fe_4O_{12}$ can be synthesized at 8–15 GPa and 1200–1500 K. For instance, figure 2(a) shows the synchrotron x-ray diffraction (SXRD) pattern of $LaCu_3Fe_4O_{12}$ (LCFO) measured at 300 K. It can be well fitted based on an A-site ordered double perovskite structure model with a cubic Im-3 space group. In the structure, A-site La and A'-site Cu are 1:3 ordered at special sites 2a (0, 0, 0) and 6b (0, 0.5, 0.5), respectively. B-site Fe occupies special site 8c (0.25, 0.25, 0.25) and O occupies site 24g (x, y, 0). The refinement for occupation factors of atoms is near unity, indicating good chemical stoichiometry.

The oxygen content can be further determined by thermogravimetric (TG) measurement as shown in Fig. 3. The compound starts to decompose at a temperature around 820 K, losing 3.25% of its mass. According to the decomposition reaction ($LaCu_3Fe_4O_{12} \rightarrow LaFeO_3 + 3/2CuFe_2O_4 + 3/2CuO + 3/4O_2$), the expected TG loss is about 3.22%, which is very close to the observed one. Therefore, oxygen content in LCFO is almost stoichiometric. Figure 3 also shows a differential thermal analysis (DTA) of LCFO. Obviously, when the temperature increases to a critical temperature (T_C) 393 K, a sharp endothermic peak is observed in the DTA curve. However, there is no change in the TG curve near T_C. These observations thus strongly suggest an intrinsic phase transition occurring at around 393 K.

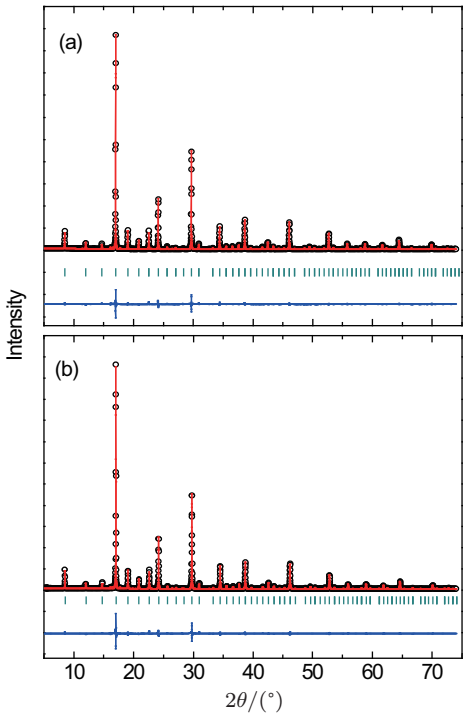


Fig. 2. (color online) SXRD patterns and the Rietveld refinement profiles of $LaCu_3Fe_4O_{12}$ at (a) 300 K and (b) 425 K. The observed (circles), calculated (red line), and difference (blue line) patterns are shown. Ticks show the positions of the Bragg reflections.[31]

To understand the origin of the phase transition at T_C, high-temperature SXRD was performed. Figure 2(b) shows the SXRD pattern of LCFO measured at 450 K ($> T_C$). Structural analysis demonstrates that the crystal symmetry above T_C is completely identical with that of the phase below T_C, suggesting that the phase transition occurring at 393 K is an isostructural one. Moreover, when the unit cell volume as a function of temperature is examined (see Fig. 4), one can find a sharp volume variation of about 1.2%, revealing the first-

order nature of this isostructural phase transition. Note that the volume change of LCFO around T_C differs from the usual thermal expansion, exhibiting anomalous shrinkage during the phase transition.

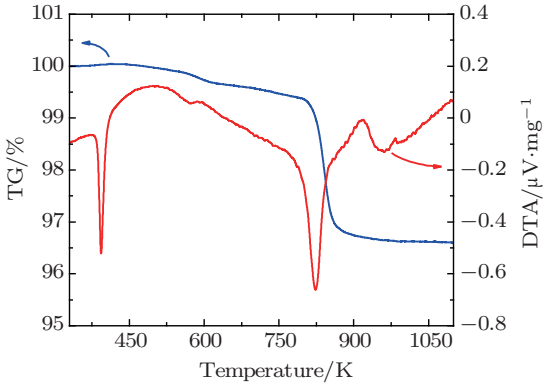


Fig. 3. (color online) Thermogravimetry and differential thermal analysis of $LaCu_3Fe_4O_{12}$.[31]

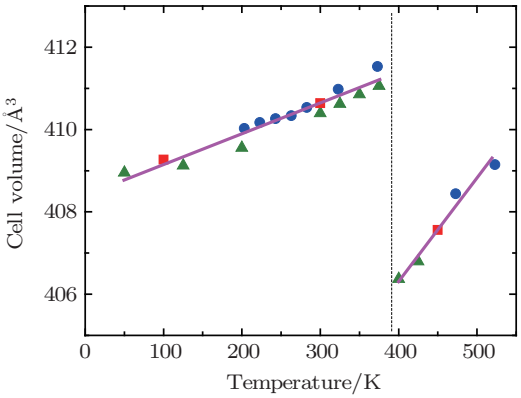


Fig. 4. (color online) Temperature dependence of the unit cell volume of $LaCu_3Fe_4O_{12}$. The data were obtained from conventional XRD (●), SXRD (■), and NPD (▲).[31]

The cell volume in the *A*-site ordered perovskite is closely related to the B–O bond length. According to structure refinement results (Table 1), the temperature dependence of Fe–O and Cu–O distances is obtained as shown in Fig. 5(a). Clearly, the Fe–O bond length sharply decreases around T_C, giving rise to the drastic volume contraction. In contrast, the Cu–O distance increases remarkably near the critical temperature. The band valence sums were calculated based on the Fe–O and Cu–O bond lengths (see Fig. 5(b)). The valence states of Fe and Cu below T_C are both close to +3, forming a $LaCu_3^{3+}Fe_4^{3+}O_{12}$ charge combination with the very rare Cu^{3+} residing at the square-planar *A*′-site. Above T_C, however, the unusually high Cu^{3+} is reduced to a Cu^{2+}, whereas the valence state of Fe becomes much higher than +3. On account of the stoichiometric composition of $LaCu_3Fe_4O_{12}$, the high-temperature charge combination should change to $LaCu_3^{2+}Fe_4^{3.75+}O_{12}$, which is the same as that of other *A*-site ordered perovskites such as $LaCu_3^{2+}Mn_4^{3.75+}O_{12}$ and $BiCu_3^{2+}Mn_4^{3.75+}O_{12}$.[25,26]

Table 1. Crystal structure parameters of $LaCu_3Fe_4O_{12}$, determined by Rietveld refinements of SXRD and NPD data.

$LaCu_3Fe_4O_{12}$	SXRD	SXRD	NPD	NPD
T/K	300	450	300	425
space group	*Im*-3	*Im*-3	*Im*-3	*Im*-3
Z	2	2	2	2
a/Å	7.43283(4)	7.41420(6)	7.4351(1)	7.4345(8)
V/Å^3	410.641(7)	407.561(9)	411.02(2)	410.9(1)
O_x	0.3111(3)	0.3070(4)	0.3110(2)	0.302(3)
O_y	0.1711(4)	0.1764(4)	0.1690(3)	0.174(3)
U_{iso}(La/Bi)/10^2 Å^2	0.26(2)	0.42(2)	0.5(1)	3(1)
U_{iso}(Cu)/10^2 Å^2	1.09(2)	1.48(3)	1.19(6)	2.9(5)
U_{iso}(Fe)/10^2 Å^2	0.14(2)	0.22(2)	0.79(3)	6.7(6)
U_{iso}(O)/10^2 Å^2	0.36(7)	0.67(8)	0.80 (3)	4.9(4)
Cu–O/4 Å	1.895(2)	1.939(3)	1.885(2)	1.96(2)
	2.819(3)	2.794(4)	2.834(2)	2.84(6)
	3.364(6)	3.307(7)	3.377(2)	3.30(4)
Fe–O/6 Å	2.0007(9)	1.978(1)	2.0059(7)	1.981 (5)
Fe–O–Fe/(°)	136.5(1)	139.2(2)	135.8(1)	139.5(8)
R_{wp}/%	6.70	7.71	5.09	4.54
R_p/%	4.70	5.42	4.31	3.96

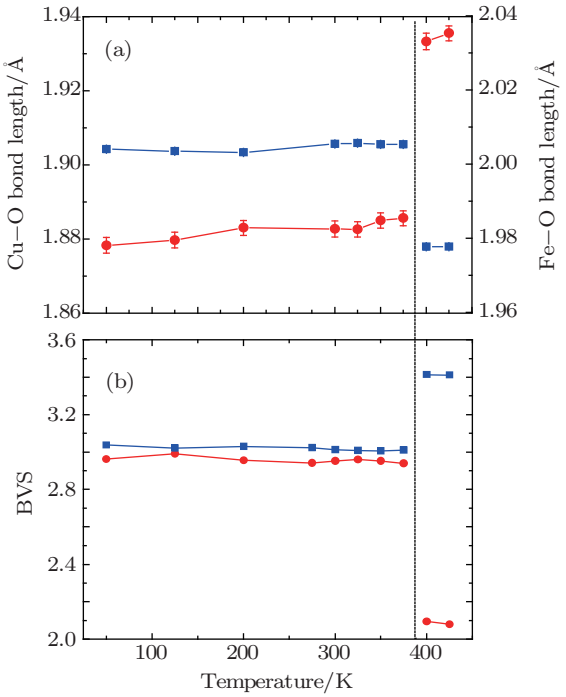


Fig. 5. (color online) Temperature dependence (a) lengths of Cu–O (●) and Fe–O (■) bonds and (b) calculated BVS values for Cu (●) and Fe (■) ions in $LaCu_3Fe_4O_{12}$.[30]

The valence state change of Fe can be confirmed further by Mössbauer spectrum (MS) measurements. Figure 6 shows the MS results of LCFO collected at different temperatures. Below T_C (e.g., at 4.2 K and 298 K), the MS very consistently shows one spectral feature, a single magnetic sextuplet. The isomer shift (IS) values obtained at 4.2 K and 298 K are respectively 0.47 and 0.34 mm/s, typical values for Fe^{3+} with a high-spin configuration,[41,42] further confirming the charge combination of $LaCu_3^{3+}Fe_4^{3+}O_{12}$ below the transition temperature. In contrast, the MS measured above T_C displays an essentially different feature, which consists of a

paramagnetic singlet, as shown in Fig. 6(c). The related IS value is fitted to be 0.17 mm/s, which is an intermediate value between ~ 0.07 mm/s for an Fe^{4+} state and ~0.35 mm/s for an Fe^{3+} state,[43,44] in accordance with the high-temperature $LaCu_3^{2+}Fe_4^{3.75+}O_{12}$ charge combination. The changes in the valence state strongly indicate the occurrence of intermetallic charge transfer between the A'-site Cu and the B-site Fe ions ($3Cu^{3+} + 3e \rightarrow 3Cu^{2+}$; $4Fe^{3+} - 3e \rightarrow 4Fe^{3.75+}$).

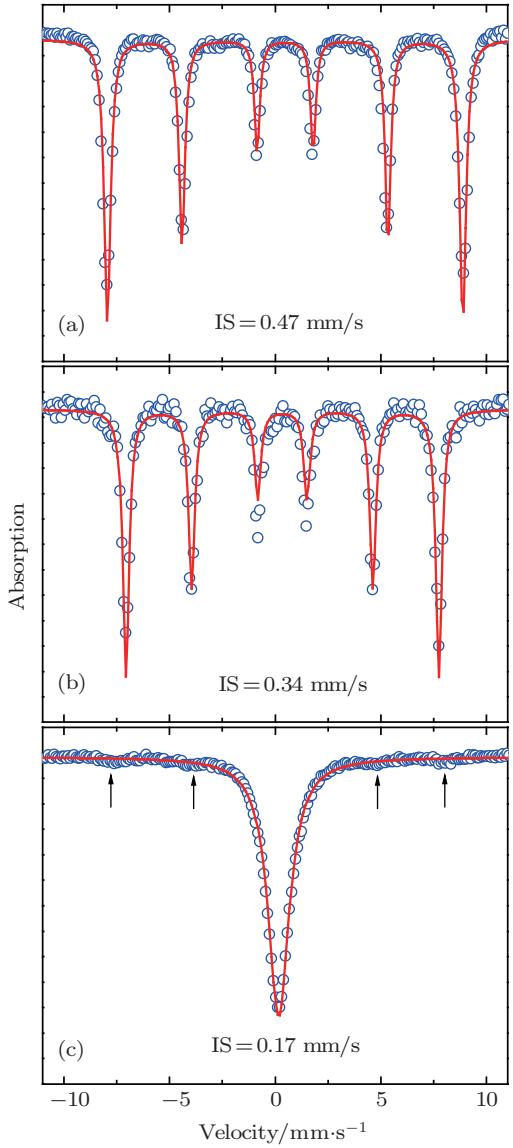


Fig. 6. (color online) Mössbauer spectra of $LaCu_3Fe_4O_{12}$ at (a) 4.2 K, (b) 298 K, and (c) 423 K. Arrows in panel (c) show spectral features due to a small amount of α-Fe_2O_3 impurity.[31]

The first-order charge-transfer transition changes the electronic configurations of Cu and Fe ions simultaneously, so in addition to the sharp variation in unit cell configuration, the magnetism and electrical transport properties are also expected to change significantly. Figure 7(a) shows the temperature dependence of magnetic susceptibility. A dramatic anomaly is obvious where temperature passes T_C, suggesting the presence of a magnetic phase transition accompanying the charge transfer. Actually, the observed magnetic sextuplet in the MS below T_C indicates long-range spin ordering of Fe^{3+} ions, while the singlet above T_C demonstrates the nonmagnetic nature. Furthermore, the temperature dependent hyperfine field (HF) obtained based on the MS measurements also agrees with the spin order-to-disorder transition (Fig. 7(b)). The exact zero HF value above T_C confirms the paramagnetic state. However, the HF increases sharply when the charge combination changes from the high-temperature $LaCu_3^{2+}Fe_4^{3.75+}O_{12}$ to the low-temperature $LaCu_3^{3+}Fe_4^{3+}O_{12}$, reflecting the development of long-range spin ordering below T_C. Taking into account the linear magnetization behavior in the spin ordered $LaCu_3^{3+}Fe_4^{3+}O_{12}$ phase, shown in the inset in Fig. 7(a), long-range antiferromagnetic (AFM) ordering is expected.

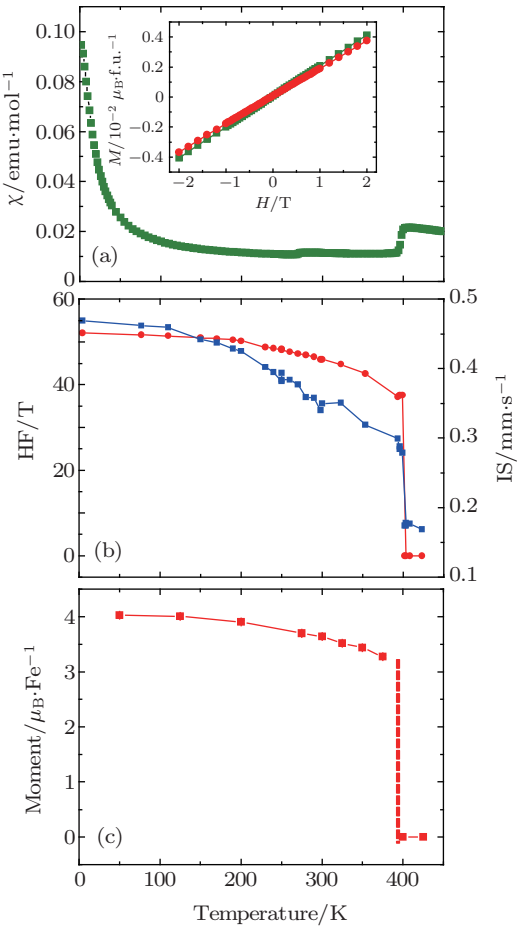


Fig. 7. (color online) Temperature dependence of (a) magnetic susceptibility χ measured at an applied field of 0.1 T, (b) hyperfine field HF (●) and isomer shift IS (■), and (c) magnetic moment of Fe obtained form NPD analysis of $LaCu_3Fe_4O_{12}$. The inset in panel (a) shows the linear magnetization behavior at 300 K (●) and 200 K (■).[30]

To further confirm the charge-transfer-induced spin order transition, neutron powder diffraction (NPD) was performed at different temperatures (see Fig. 8). The NPD pattern measured at 425 K (Fig. 8(b)) can be fitted well based on the cubic Im-3 crystal structure model as mentioned before, and no magnetic diffraction peak is visible above T_C. Below the critical temperature, however, strong magnetic contributions are

observed, as clearly seen by the 111 and 113 magnetic Bragg reflections (Fig. 8(a)). The refinement reveals a magnetic superstructure with a (1/2 1/2 1/2) propagation vector of the cubic cell, producing a G-type AFM structure, where each Fe^{3+} spin aligns antiparallel to the six nearest neighbors, as shown in Fig. 9. This AFM ordering is also consistent with the linear magnetization behavior (inset in Fig. 7(a)). The refined magnetic moments of the *B*-site Fe are $4.03(2)\mu_B$ and $3.28(3)\mu_B$ at 50 K and 375 K, respectively (Fig. 7(c)). Both of them are reduced from the ideal value of $5.0\mu_B$ for a high-spin Fe^{3+} ($S = 5/2$), probably implying some Fe–O covalency effects. No magnetic contribution from the square-planar-coordinated 6*c* site is found. Because the square-planar-coordinated Cu results in considerable energy splitting between the $d_{x^2-y^2}$ and $d_{3z^2-r^2}$ orbitals, the 3d electrons in Cu^{3+} ($3d^8$) ions fully occupy the d_{xz}, d_{yz}, d_{xy}, and $d_{3z^2-r^2}$ orbitals, making the $d_{x^2-y^2}$ orbital empty with a total spin $S = 0$. The AFM ordering thus originates from the *B*-site Fe^{3+} only.

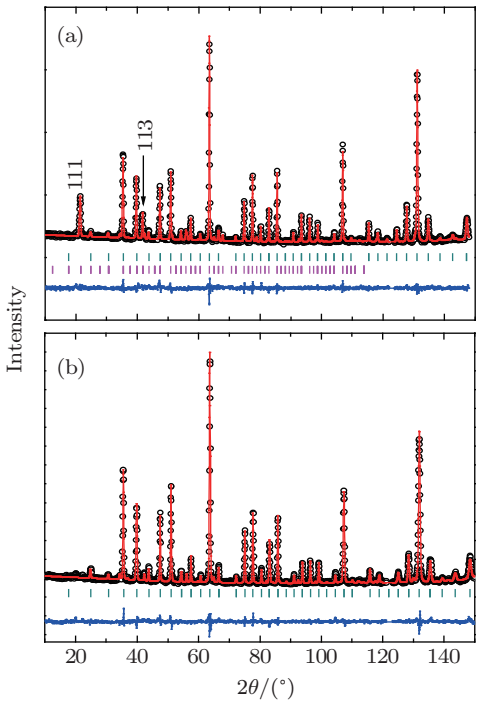


Fig. 8. (color online) The NPD patterns and Rietveld refinement profiles of $LaCu_3Fe_4O_{12}$ at (a) 300 K and (b) 425 K. The observed (circles), calculated (red line), and difference (blue line) patterns are shown. Green ticks show the positions of the Bragg reflections, and pink ticks in panel (a) show the positions of magnetic reflections from the G-type antiferromagnetic ordering of the *B*-site spins.[31]

In the *A*-site ordered perovskites, the $A'O_4$ units are spatially isolated from each other, so the electrical conductivity must be dominated by the corner-sharing BO_6 octahedra (see Fig. 1(c)). As shown in Fig. 10, the low-temperature AFM phase with Fe^{3+} displays insulating behavior. The temperature dependence of resistivity between 100 K and 300 K can be fitted well based on a Mott 3D variable-range hopping (VRH) model: $R(T) = R_0 \exp(T_0/T)^{1/4}$ (inset of Fig. 10). However, when the *B*-site Fe^{3+} is changed to a mixed $Fe^{3.75+}$, an insulator-to-metal transition is observed at T_C. The observed thermal hysteresis in resistance is also consistent with the first-order nature of the intermetallic charge transfer transition.

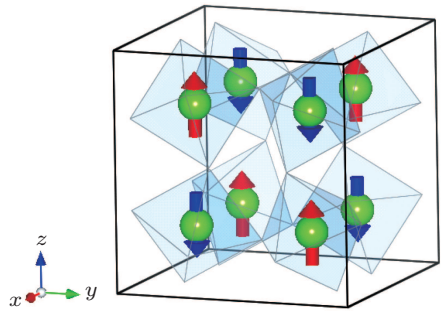


Fig. 9. (color online) The G-type antiferromagnetic structure of *B*-site Fe^{3+} spins in $LaCu_3Fe_4O_{12}$. Only magnetically ordered Fe^{3+} ions are shown. Spins are drawn along the [001] direction because the exact orientation of the magnetic moments cannot be determined by NPD.[32]

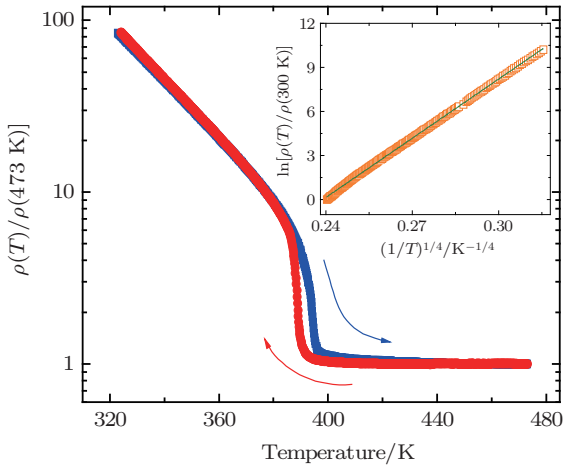


Fig. 10. (color online) Temperature dependence of normalized resistivity of $LaCu_3Fe_4O_{12}$. Inset shows the result obtained by fitting data in the temperature range between 100 K and 300 K to a 3D VRH model.[31]

In addition to LCFO, the Cu–Fe intermetallic charge transfer is observed in other $ACu_3Fe_4O_{12}$ systems, systems with A = Pr, Nd, Sm, Eu, Gd, Tb, or Bi, giving rise to similar interrelated changes in unit cell, magnetism and electrical conductivity.[31,34,35] Moreover, with decreasing size of the ion at the *A*-site, the charge-transfer critical temperature gradually decreases. When high pressure is applied to tune the unit cell volume, a pressure-induced charge transfer is found to occur in LCFO at room temperature.[33] Note that if another rare earth ion with smaller ionic radius, such as Dy, Ho, Er, Tm, Yb, Lu or Y, is substituted at the *A*-site, charge disproportion of iron ions ($8Fe^{3.75+} \rightarrow 3Fe^{5+} + 5Fe^{3+}$) takes place instead of Cu–Fe intermetallic charge transfer ($3Cu^{3+} + 4Fe^{3+} \rightarrow 3Cu^{2+} + 4Fe^{3.75+}$).[35,45] It has been reported that the strength of the crystal-field splitting and the relative energy ordering between Cu $3d_{xy}$ and Fe 3d states are the

key parameters determining the intermetallic charge transfer (charge disproportionation) in $ACu_3Fe_4O_{12}$ compounds with light (heavy) rare earth metals.[46]

3. Magnetoelectric multiferroicity in a cubic perovskite $LaMn_3Cr_4O_{12}$

Magnetoelectric (ME) multiferroicity with coupled ferroelectric and magnetic orders has received much attention due to its great potential for numerous applications.[47–54] Perovskites are one of the most important material systems for multiferroic study. Since the discovery of multiferroic behavior in perovskites $BiFeO_3$ and $TbMnO_3$,[48,49] a many multiferroic materials with different physical mechanisms have been found in the last decade.[55–59] Among them, the spin-induced multiferroics have received the most attention because their ferroelectricity is induced by magnetic structures, leading scientists to expect a strong ME coupling.[60–62] Several theories such as the spin-current model (or inverse Dzyaloshinskii–Moriya interaction), exchange striction mechanism and d–p hybridization mechanism have been proposed to account for the spin-induced ferroelectricity in ME multiferroics by special spin textures such as non-collinear spiral spin structures and collinear E-type AFM structure with zigzag spin chains.[63–67] It is well known that a cubic perovskite lattice is unfavorable for ferroelectricity due to the existence of an inversion center. However, the total symmetry for an ME multiferroics reflects the crystal and magnetic symmetries together. Therefore, in principle, it is possible to find ME multiferroics in a cubic perovskite system if the system's magnetic structure breaks the space inversion symmetry. Nevertheless, such an intriguing case was never found in previous studies. The $AA'_3B_4O_{12}$-type A-site ordered perovskite provides an opportunity for researching ME multiferroics in a cubic lattice. Since both A' and B sites accommodate magnetic transition-metal ions, multiple magnetic and electrical interactions may develop, while the crystal structure can be finely tuned by selecting appropriate A' and B elements to maintain the cubic lattice.[24,30,68–70]

In this section, a spin-driven multiferroic phase with strong ME coupling effects in the A-site ordered perovskite $LaMn_3Cr_4O_{12}$ (LMCO) with cubic symmetry will be described. The unique multiferroic behavior in this cubic perovskite originates from a nontrivial effect involving the interactions between two magnetic sublattices. The present study not only provides the first example of multiferroics in a cubic perovskite system but also presents new insights into the physical mechanisms of multiferroics.

LMCO can be prepared by using high pressure and high temperature conditions, as detailed in Ref. [28]. Temperature dependent XRD shows that this compound always possesses an A-site ordered perovskite structure with cubic space group Im-3 from 23 K to 293 K (Fig. 11). The stability of this long-range cubic crystal structure is also confirmed by low-temperature (10–300 K) Raman scattering as shown in Fig. 12(a).

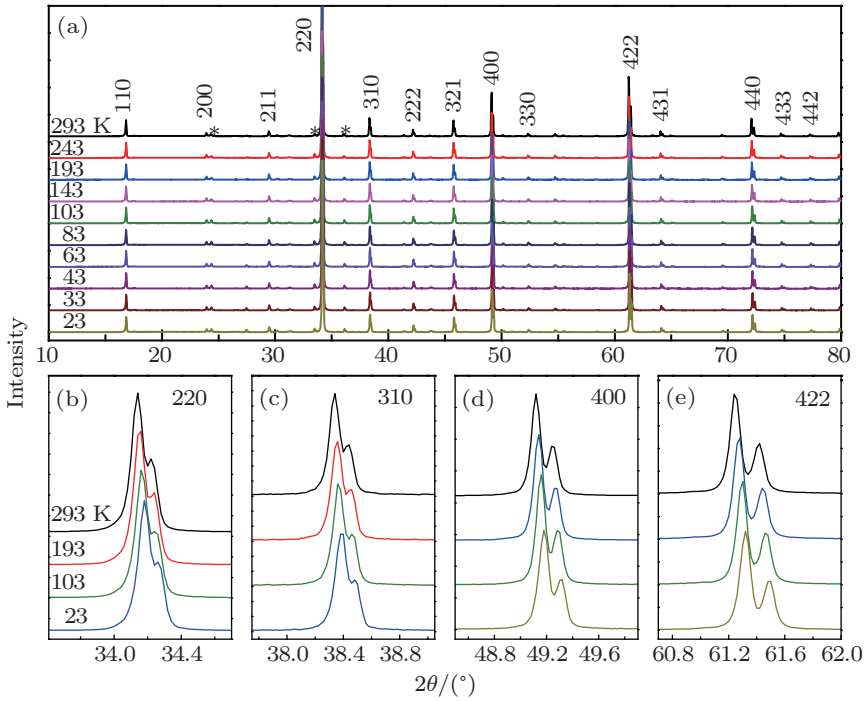


Fig. 11. (color online) (a) Temperature dependent x-ray diffraction of $LaMn_3Cr_4O_{12}$. Diffraction peaks were indexed based on space group Im-3. Stars show the diffraction peaks originating from a small amount of Cr_2O_3 impurity. (b)–(e) The enlarged views for several representative diffraction peaks. No structural phase transition occurs as temperature decreases from 293 K to 23 K.

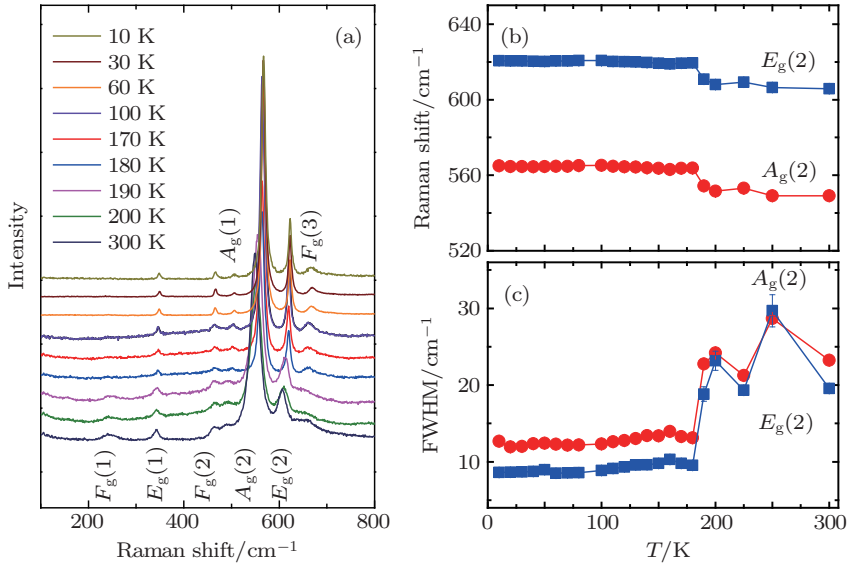


Fig. 12. (color online) (a) Raman spectra measured at different temperatures for $LaMn_3Cr_4O_{12}$. No long-range structural phase transition is observed between 300 K and 10 K. Temperature dependence of (b) Raman shift and (c) the full width at half maximum (FWHM) for the two strongest Raman modes $A_g(2)$ and $E_g(2)$. Anomalies around 180 K may indicate local structural changes, as described in text.

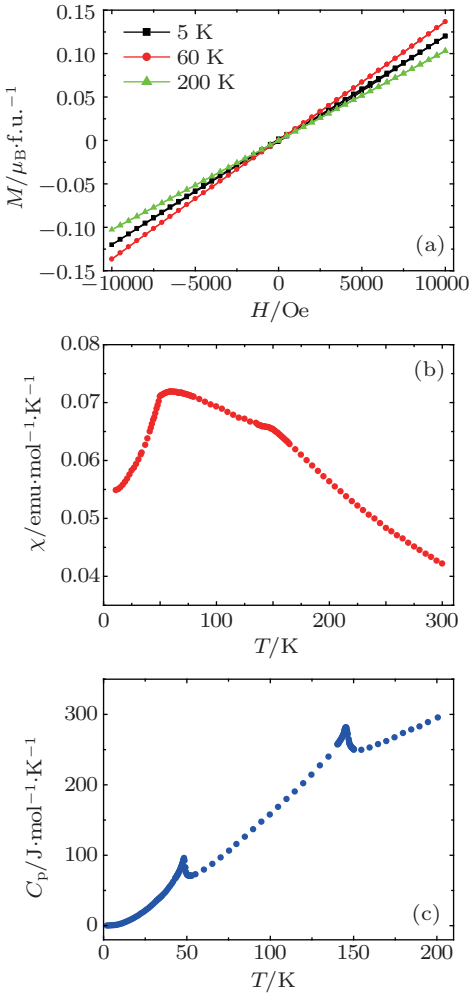


Fig. 13. (color online) (a) Magnetic field dependence of magnetization measured at different temperatures. The linear magnetization behaviors are consistent with the collinear G-type antiferromagnetic structure of $LaMn_3Cr_4O_{12}$ as revealed by neutron powder diffraction. (b) Temperature dependence of susceptibility χ of LMCO. (c) Temperature dependence of specific heat C_P of LMCO.

Magnetic susceptibility and specific heat measurements reveal two AFM transitions in LMCO, occurring at $T_{Mn} \sim 50$ K and $T_{Cr} \sim 150$ K, respectively (Fig. 13). To clarify the origin of these two AFM phase transitions, NPD was performed at different temperatures. The NPD data shown in Fig. 14 demonstrates that the cubic *Im*-3 crystal structure persists down to 2 K, in agreement with the low-temperature XRD and Raman results. Meanwhile, based on the temperature dependence of the magnetic peaks (111) and (100) (Figs. 15(a) and 15(b)), the NPD results confirm that the spin orderings of the Mn and Cr sublattices lead to the AFM transitions at $T_{Mn} \sim 50$ K and $T_{Cr} \sim 150$ K, respectively. Furthermore, the NPD refinements produce collinear G-type AFM spin structures for both the A'-site Mn-sublattice and the B-site Cr-sublattice, with the propagation vector of (111)/(100) for the Cr/Mn-sublattice and the spin orientations most probably along the equivalent [111] direction (Fig. 16). This collinear AFM spin configuration is consistent with the linear magnetization behaviors observed at different temperatures, shown in Fig. 13(a).

Figure 17(a) shows the temperature dependence of the dielectric constant (ε). Corresponding to the AFM phase transition occurring at T_{Mn}, ε also displays a sharp anomaly. Moreover, this dielectric variation is independent of frequency, implying the possibility of a ferroelectric phase transition coupled with AFM ordering of the Mn spins. Thus, the ME coupling may occur at the onset of T_{Mn} in the cubic perovskite LMCO. Looking further, we see another broadening and frequency-dependent dielectric anomaly at about 110 K for 10 kHz and 155 K for 1 MHz. This relaxation behavior is reminiscent of a ferroelectric transition, probably originating from local structure inhomogeneity and/or some extrinsic effects, as will be discussed later.[73]

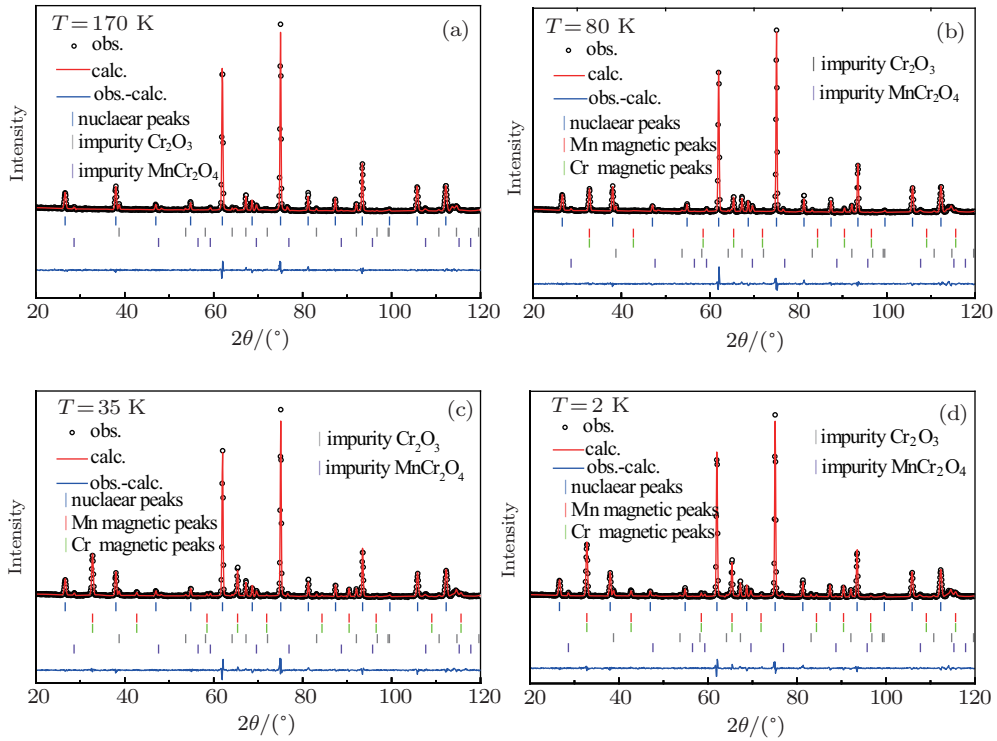


Fig. 14. (color online) Rietveld refinements for neutron powder diffraction data of $LaMn_3Cr_4O_{12}$ collected at (a) 170 K, (b) 80 K, (c) 35 K, and (d) 2 K. Small amounts of Cr_2O_3 and $MnCr_2O_4$ impurity phases (< 5 wt%) were observed.

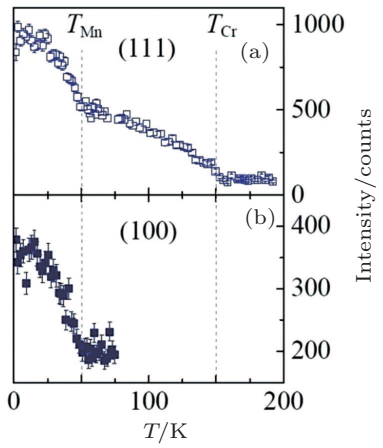


Fig. 15. (color online) Temperature dependence of integrated NPD intensities of (111) (a) and (100) (b) peaks, respectively.

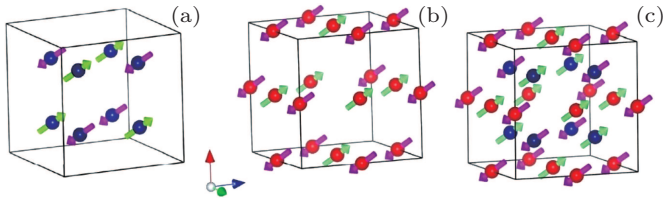


Fig. 16. (color online) G-type AFM structures of the *B*-site Cr-sublattice (a) and the *A*′-site Mn-sublattice (b), both with spin orientation along the [111] direction. (c) A complete set of spin alignment composed of Cr and Mn spins below T_{Mn}. For clarity, La and O atoms are omitted in the structures. Blue ball: Cr atom; red ball: Mn atom.

These two ferroelectric phase transitions were further studied by measuring pyroelectric current (I_p) to derive the ferroelectric polarization (P) with both positive and negative electric (E) poling procedures from 200 K down to 5 K, as shown in Figs. 17(b) and 17(c). Obviously, the I_p and P are completely switchable by the poling E reversal. The most striking finding is that the Mn spin ordering transition is coupled with a sharp change in both I_p and P at T_{Mn} (Figs. 17(b) and 17(c) and the insets), strongly indicating that the presence of this low-temperature ferroelectric phase transition (FE1) is closely related to the magnetic ordering of the Mn sublattice, in agreement with the dielectric constant measurements. In addition, in the high temperature region, I_p and P were found to emerge gradually below about 180 K, and then a broad peak in I_p appears near 125 K (Fig. 17(b)). Since these two characteristic temperatures (180 K and 125 K) differ from the value of T_{Cr} (150 K), the associated ferroelectric phase (FE2) seems to be of non-magnetic origin.

Note that the drastic changes of I_p at T_{Mn} are not a single peak or dip but unusual dip-peak features and vice versa for the +poled and −poled curves, respectively (inset of Fig. 17(b)). Accordingly, the obtained $P(T)$ curves slightly decreases and then increases or vice versa for +poled or −poled on cooling around T_{Mn} (inset of Fig. 17(c)). This implies that two independent polarizations are superposed below T_{Mn}. To prove this point, two different poling E schemes were performed, passing either 180 K or T_{Mn} (= 50 K) only. In sharp contrast to the dip-peak features in I_p when poling E across both T_{Mn} and 180 K, only a single dip (200–75 K, +poled) or peak (75–30 K, +poled) in I_p was observed in each poling scheme,

respectively, as shown in Figs. 18(a) and 18(b). Correspondingly, the obtained net polarization changes ($\Delta P = P(T) - P$ (50 K)), which represent the influence of Mn ordering upon the P values, show negative values when E is applied only across 180 K, whereas positive ΔP values are obtained with E applied only across $T_{\rm Mn}$, as shown in Fig. 18(c). The single dip in $I_{\rm p}$ (200–75 K, +poled) means that, although the FE2 phase sets in at a temperature much higher than $T_{\rm Mn}$, the spin ordering of Mn ions still causes a decrease of in the magnitude of P in this phase. More interestingly, the peak in $I_{\rm p}$ (75–30 K and +poled) reveals that the FE1 phase, which develops at $T_{\rm Mn}$, is a ferroelectric phase that is independent of the FE2 phase. Since the FE1 phase strongly couples with the AFM ordering of the Mn-sublattice, the present cubic perovskite LMCO can be regarded as a new case of spin-driven multiferroics below $T_{\rm Mn}$.

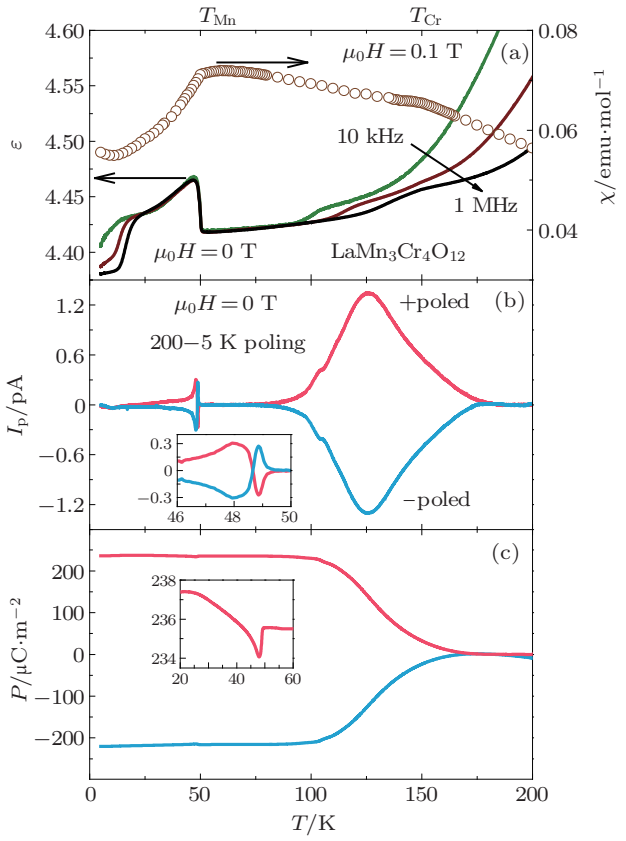


Fig. 17. (color online) Temperature dependence of (a) dielectric constant ε and magnetic susceptibility χ, (b) pyroelectric current $I_{\rm p}$ and (c) ferroelectric polarization P in both +poled and −poled conditions. The ε and $I_{\rm p}$ were measured without magnetic field. Insets of panels (b) and (c) show enlarged views near 50 K.[36]

To further confirm that the observed pyroelectric signals come from intrinsic ferroelectricity instead of a plausible space charge effect, different external magnetic fields are applied to measure the pyroelectric and dielectric properties. Considerable anisotropic ME and magnetodielectric effects are found in these two FE phases at and below $T_{\rm Mn}$. As shown in Fig. 19(a), when an external magnetic field $H||E$ is applied up to 12 T in the poling and measuring processes, the absolute values of $I_{\rm p}$ near $T_{\rm Mn}$ are enhanced by about one order of magnitude for both phases. The calculated $|\Delta P|$ values in both FE phases also increase from ~ 15 μC/m^2 to ~ 68 μC/m^2 at 30 K (Fig. 19(b)). In the $H \perp E$ configuration, however, the $I_{\rm p}$ near $T_{\rm Mn}$ is found to be completely suppressed above 7 T field (not shown here).

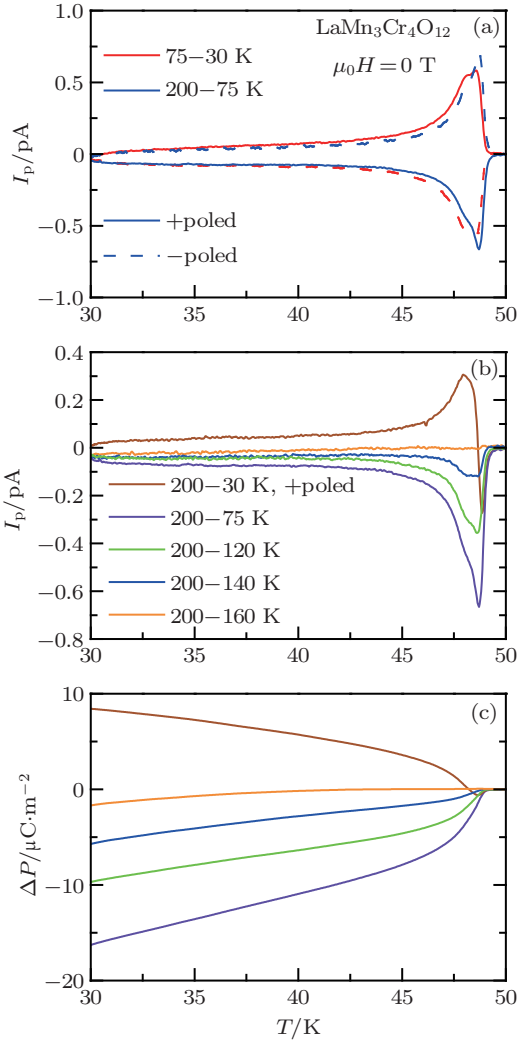


Fig. 18. (color online) Poling procedure dependence of electric behaviors below $T_{\rm Mn}$. (a) Temperature dependence of pyroelectric current $I_{\rm p}$ by +poled and −poled under 200–75 K and 75–30 K poling conditions. Temperature dependence of (b) $I_{\rm p}$ and (c) the difference of polarization $\Delta P(= P(T) - P(50\ {\rm K}))$ after being +poled from 200 K down to the selected temperatures. The ΔP is obtained by integration of $I_{\rm p}$ in panel (b) as a function of time. As shown in panel (b), a dip-peak feature is observed when E passes through both 180 K and $T_{\rm Mn}$, whereas only a single dip is observed when E is turned off at temperatures higher than $T_{\rm Mn}$. Therefore, the dip in $I_{\rm p}$ at $T_{\rm Mn}$ must be contributed by the FE2 phase, and the peak in $I_{\rm p}$ at $T_{\rm Mn}$ originates from the FE1 phase. The corresponding negative ΔP indicates that electric polarization of the FE2 phase decreases in magnitude below $T_{\rm Mn}$.

Similarly, the dielectric constant ε also shows significant changes under magnetic field at and below $T_{\rm Mn}$. For the $H||E$ configuration, the sudden jump in ε around $T_{\rm Mn}$ for $\mu_0 H = 0$ changes into a sharp peak for $\mu_0 H \geq 3$ T (Fig. 20(a)). By comparison, the $H \perp E$ configuration shows a remarkably smaller

dielectric jump at T_{Mn}, so much so that almost no dielectric anomaly is observed with field above 7 T (Fig. 20(b)), consistent with the complete suppression of electric polarization at this H and E configuration under high field mentioned above. On the other hand, however, with increasing magnetic field, there is no remarkable change in ε above T_{Mn} in either the $H||E$ or the $H\perp E$ configuration, revealing that the FE1 and FE2 phases have different origins. Anyway, our magnetic-field dependent measurements show that the FE1 phase has strong anisotropic H dependent behavior, excluding any extrinsic origin of the space charge for this multiferroic phase.

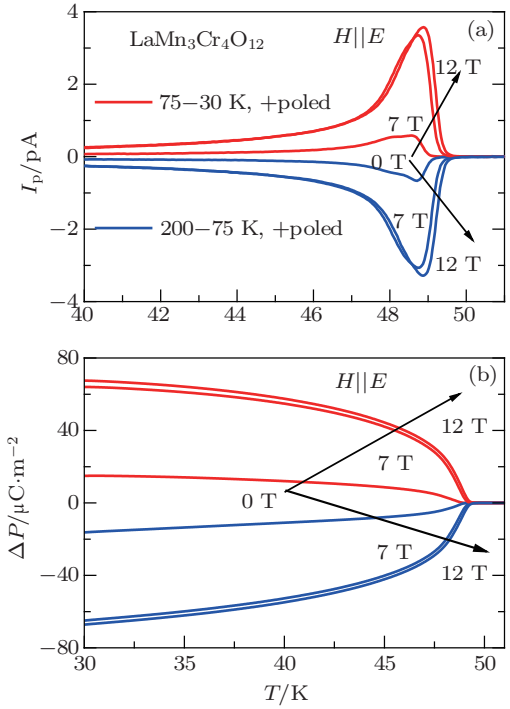


Fig. 19. (color online) (a) Temperature dependence of I_p and (b) difference of polarization ΔP under different poling conditions and different magnetic fields below 50 K.[36]

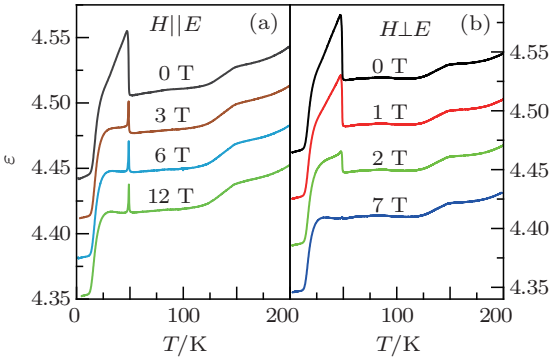


Fig. 20. (color online) Temperature dependence of ε measured at 1 MHz and different magnetic fields with $H||E$ and $H\perp E$ configurations, respectively. Data have been shifted for clarity.[36]

Note that, as can be seen from the XRD and NPD patterns (Figs. 11 and 14), small amounts of Cr_2O_3 and $MnCr_2O_4$ impurity phases (< 5 wt%) were found in our high-pressure product. Although these two phases exhibit multiferroic behaviors, they do not affect the intrinsic physical properties of LMCO. Specifically, Cr_2O_3 displays an ME effect below 307 K,[67] but this phase transition temperature is much different from both the T_{Mn} ($= 50$ K) and the T_{Cr} ($= 150$ K) observed in our LMCO (Fig. 13). Moreover, there is no visible polarization above 180 K (Figs. 17(b) and 17(c)), indicating that the magnetic and electric transitions, as well as the ME coupling, of LMCO are not related to the Cr_2O_3 impurity. In addition, $MnCr_2O_4$ shows a sharp ferrimagnetic transition at 43 K and exhibits significant spontaneous magnetization with a saturated moment of about $1.0\mu_B$ f.u.$^{-1}$ at 5 K.[72] In the present LMCO, however, there is no magnetic anomaly around 43 K (Fig. 13(a)), and the magnetic field dependence of magnetization shows a completely linear relationship at 5 K (Fig. 13(b)). Therefore, any effect of $MnCr_2O_4$ on the intrinsic physical properties of LMCO can also be safely ruled out. Recently, a centrosymmetric perovskite, $SmFeO_3$ has been reported to have multiferroicity that is induced by noncollinear G-type AFM order.[74] Unfortunately, however, this reported ferroelectricity was later disproven by theoretical work[75] and other experiments.[76] In particular, Kuo *et al.*[76] suggested that magnetoelastic coupling can give rise to artificial pyroelectric current, as has been observed in $SmFeO_3$. However, this is not the case for the LMCO sample. Magnetoelastic-coupling induced pyroelectric current usually is not switchable by poling electric field, as pointed out by Johnson *et al.* for the case of $CaBaCo_4O_7$.[77] Nevertheless, the pyroelectric current of LMCO can be reversed by poling electric field. Moreover, the sign of the magnetoelectric coefficient $(\mathrm{d}P/\mathrm{d}H)$ can also be reversed by changing the direction of the poling electric field. These two facts completely rule out the magnetoelastic-coupling mechanism in LMCO. Therefore, the ferroelectricity observed in LMCO below $T_{Mn} = 50$ K must be intrinsic in origin.

Next we discuss some possible mechanisms responsible for the low-temperature Mn spin ordering induced ferroelectricity in the cubic perovskite LMCO. First, both the inverse Dzyaloshinskii–Moriya interaction and the spin-current model, both of which are related to the cross products of spins, are excluded due to the collinear spin configuration of LMCO (Figs. 16(a)–16(c)). The exchange striction mechanism-induced electric polarization is related to the dot product of a pair of spins, which is independent of the spin orientations if the two spins are always parallel or antiparallel with each other. In contrast, based on the magnetic point group analysis and theoretical calculations to be shown later, the polarization direction of FE1 phase is always simultaneously changed with the spin orientations (in one of the equivalent [111] directions). This means that the exchange striction mechanism does not contribute to the polarization in FE1 phase if there is

any. As a consequence, these conventional ME mechanisms simply cannot explain the present ferroelectric behaviors.

In the temperature region of $T_{Mn} < T < T_{Cr}$, the Cr sublattice is ordered in a G-type AFM manner with spin orientation along the [111] direction (Fig. 16(a)). Since the crystal space group is *Im*-3, the magnetic point group must be a non-polar ***–3′*** group with a space inversion center. At $T < T_{Mn}$, the Mn sublattice is also ordered in a G-type AFM structure with non-polar ***–3*** group as its own magnetic point group (Fig. 16(b)). Therefore, no polarization can be induced by either Cr or Mn spin ordering alone. However, when the Mn and Cr sublattices are considered together below T_{Mn}, the system magnetic point group is polar group ***3*** (Fig. 16(c)), which allows polarity along the spin direction. This suggests that the ferroelectric polarization of the FE1 phase most probably arises from the Mn and Cr spin configurations together, ruling out any possibility of a single spin mechanism, e.g., the d–p hybrid model.[66]

Density functional theory calculations have been performed to better understand the spin-driven ferroelectricity of the FE1 phase. The calculated density of states with a band gap at about 1.75 eV reveals the insulating nature of LMCO (see Fig. 21). The calculated local moments for the Mn ($3.907\mu_B$) and Cr ($2.799\mu_B$) ions also agree with the NPD refinement results (Table 2). The ferroelectric polarization was calculated using the Berry phase method.[78] The experimental magnetic orders were adopted and the structure was relaxed starting from the experimental one. The results show: 1) Without considering the spin–orbit coupling (SOC) of the magnetic ions, the calculated ferroelectric polarization for the experimental magnetic ground state is exactly zero in the FE1 phase; 2) If the SOC is considered, with all spins pointing parallel or antiparallel to the [111] axis, as the NPD study suggested, even the exact high-symmetric structure can induce a small but nonzero ferroelectric polarization ~ 3.4 C/m^2 along the [111] direction. This result, without any contribution from ionic displacement, is the pure electronic polarization; 3) The direction of pure electronic polarization can be switched by rotating the magnetic axis. These results support excluding any possible contribution from inaccuracy of the ionic relaxation calculation, and support the proposal that the intrinsic ferroelectricity is caused by the spin ordering; 4) When the ionic positions are further relaxed with SOC considered, the model gives a total polarization up to ~ 7.5 μC/m^2, still along the [111] axis. Although this small value may be not very precise due to the inaccuracy of ionic displacements, the value is comparable in order of magnitude with experimental observations at zero field (~ 15 μC/m^2, see Fig. 18(c)), and also consistent with magnetic symmetry analysis, in that the ground state magnetic structure is polarized. Note that since the three conventional mechanisms for spin-driven ferroelectricity have been shown not to be applicable in the present cubic perovskite system, other, more exotic mechanisms involving the relativistic exchange interactions are plausible, and they generate only a moderate polarization.

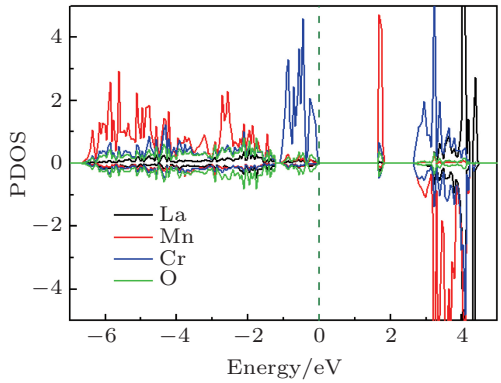


Fig. 21. (color online) DFT results with dual G-type antiferromagnetism (without SOC). Projected density of states (PDOS) for each atom species is shown. The calculated band gap (~ 1.75 eV) reveals the insulating nature of $LaMn_3Cr_4O_{12}$.

Table 2. Refined structural parameters from the NPD data of $LaMn_3Cr_4O_{12}$ at different temperatures. Space group: *Im*-3 (No. 204); atomic positions: La 2*a* (0, 0, 0), Mn 6*b* (0, 0.5, 0.5), Cr 8*c* (0.25, 0.25, 0.25), O 24*g* (0, y, z).

$LaMn_3Cr_4O_{12}$	2 K	35 K	80 K	170 K
a/Å	7.39805(9)	7.3988(1)	7.3996 (1)	7.4028(1)
y(O)	0.3104(4)	0.3096(4)	0.3099(4)	0.3102(3)
z(O)	0.1771(4)	0.1765(5)	0.1767 (4)	0.1757(4)
U_{iso}(O)	0.004(2)	0.004(2)	0.004(2)	0.004(2)
U_{iso}(La)	0.009(3)	0.005(3)	0.008(3)	0.009(3)
U_{iso}(Mn)	0.040(3)	0.036(3)	0.037(3)	0.032(3)
U_{iso}/(Cr)	0.054(3)	0.055(3)	0.048(3)	0.048(3)
d_{Mn-O}/4 Å	1.919(3)	1.921(3)	1.921(3)	1.915(2)
d_{Cr-O}/6 Å	1.978(3)	1.978(4)	1.978(3)	1.981(5)
d_{La-O}/12 Å	2.644(3)	2.637(3)	2.639(3)	2.639(1)
$\angle_{Cr-O-Cr}$/(°)	138.52(4)	138.54(5)	138.55(4)	138.14(4)
M_{Mn}/μ_B	3.40(8)	2.66(9)	0	0
M_{Cr}/μ_B	2.89(6)	2.81(6)	2.50(3)	0
R_{Bragg}/%	1.60	3.70	2.79	2.88
χ^2	1.81	1.77	1.73	1.68

As for the FE2 phase, since the pyroelectric current emerges above T_{Cr} and exhibits a broad peak at about 125 K, its origin is clearly not related to any spin ordering. Such a feature, on one hand, may be ascribed to an extrinsic effect such as space charges trapped at the grain boundaries or possible defects, as reported elsewhere.[79,80] On the other hand, some ABO_3 perovskites like $YCrO_3$ and $SmCrO_3$ with Cr^{3+} ions at the *B* site reportedly display similar electric polarizations above their AFM temperatures.[81,82] Neutron pair distribution function (PDF) was used to illustrate that this type of polarization originates from a "local non-centrosymmetric effect" caused by local displacement of the second-order Jahn–Teller Cr^{3+} cations, whereas the macroscopic crystal structure was unchanged, remaining centrosymmetric. In the present LMCO, although the long-range crystal structure is stable down to 2 K, similar local displacements of Cr^{3+} cations are

possible, as implied by the relaxation behavior of the dielectric constant in the high-temperature region (Fig. 17(a)). To further explore the possible local displacements of Cr cations in the present LMCO, low-temperature Raman scattering was performed, as presented in Fig. 12. In agreement with NPD and XRD data, the Raman spectra show no long-range crystal structure phase transition at temperatures down to 10 K. However, some Raman peaks that reflect the vibrations of CrO_6 octahedra somewhat change vibration frequency as well as full width at half maximum at around 180 K,[83] perhaps implying a local-structure origin for the FE2 phase. However, more experimental methods, such as high-resolution neutron pair distribution function, are needed to clarify the exact origin of the FE2 phase.

Anyway, it should be emphasized that the ME multiferroicity found in the present LMCO with onset at about 50 K is quite unique among all the known multiferroic systems in that it occurs in a true cubic perovskite system with simple and collinear spin alignments. Due to the highly symmetric lattice and spin structures, the three major mechanisms that induce ferroelectric polarization by magnetic ordering cannot play roles. Since pure electronic polarization shows up in the FE1 phase, the cubic LMCO may become a prototype for future studies of electronic mechanisms of ferroelectricity. The present work therefore not only provides the first example of cubic perovskite multiferroics but also opens up a new arena for study of the unexpected ME coupling mechanisms.

4. Concluding remarks

In this review paper, the Cu–Fe intermetallic charge transfer in $LaCu_3Fe_4O_{12}$ and the magnetoelectric multiferroicity in $LaMn_3Cr_4O_{12}$ are described. Both compounds are prepared under high pressure and temperature, and they crystallize to *A*-site ordered perovskite structures. Due to the simultaneous changes of Cu and Fe electronic configurations, the charge transfer in LCFO gives rise to a series of interrelated phase transitions in lattice, spin, charge and orbital degrees of freedom. Although a cubic perovskite lattice is unfavorable for ferroelectricity due to the existence of an inversion center in its structure, the spin–orbit coupling effect of Cr and Mn ions plays an important role in the electric polarization of LMCO. These interesting findings are closely related to the peculiar crystal structure of *A*-site ordered perovskites, wherein both A' and *B* sites accommodate TM ions, providing multiple magnetic and electrical interactions via A'–A', A'–*B*, and/or *B*–*B* pathways. One can thus design special functional compounds by selecting appropriate transition metals at different atomic positions to modify the magnetic and transport properties. Furthermore, if a third transition metal is partially substituted in the *B* site, both *A*-site and *B*-site ordered perovskites with specific functional properties can be formed. Therefore, the present *A*-site ordered perovskites pave the way to design new functional materials and find new physics and functionalities.

Acknowledgments

The author thanks Wang X, Chai Y S, Zhou L, Yin Y Y, Saito T, Azuma M, Shimakawa Y, Sun Y, and Jin C Q for close collaboration.

References

[1] Wul B 1946 *Nature* **157** 808
[2] Shirane G, Pepinsky R and Frazer B C 1955 *Phys. Rev.* **97** 1179
[3] Matthias B and Hippel A V 1948 *Phys. Rev.* **73** 1378
[4] Weaver H E 1959 *J. Phys. Chem. Solids* **11** 274
[5] Spaldin N A, Cheong S W and Ramesh R 2010 *Physics Today* **63** 38
[6] Disseler S M, Borchers J A, Brooks C M, Mundy J A, Moyer J A, Hillsberry D A, Thies E L, Tenne D A, Heron J, Holtz M E, Clarkson J D, Stiehl G M, Schiffer P, Muller D A, Schlom D G and Ratcliff W D 2015 *Phys. Rev. Lett.* **114** 217602
[7] Schooley J F, Hosler W R and Cohen M L 1964 *Phys. Rev. Lett.* **12** 474
[8] Raub C J, Sweedler A R, Jensen M A, Broadston S and Matthias B T 1964 *Phys. Rev. Lett.* **13** 746
[9] Karppinen M and Yamauchi H 1999 *Mater. Sci. Eng., R* **26** 51
[10] Helmolt R V, Wecker J, Holzapfel B, Schultz L and Samwer K 1993 *Phys. Rev. Lett.* **71** 2331
[11] Tendeloo1 G V, Lebedev O I, Hervieu M and Raveau B 2004 *Rep. Prog. Phys.* **67** 1315
[12] Keane M A 2003 *J. Mater. Sci.* **38** 4661
[13] Kobayashi K I, Kimura T, Sawada H, Terakura K and Tokura Y 1998 *Nature* **395** 677
[14] Philipp J B, Majewski P, Alff L, Erb A and Gross R 2003 *Phys. Rev. B* **68** 144431
[15] Kato H, Okuda T, Okimoto Y, Tomioka Y, Takenoya Y, Ohkubo A, Kawasaki M and Tokura Y 2002 *Appl. Phys. Lett.* **81** 328
[16] Krockenberger Y, Mogare K, Reehuis M, Tovar M, Jansen M, Vaitheeswaran G, Kanchana V, Bultmark F, Delin A, Wilhelm F, Rogalev A, Winkler A and Alff L 2007 *Phys. Rev. B* **75** 020404
[17] Morrow R, Mishra R, Restrepo O D, Ball M R, Windl W, Wurmehl S, Stockert U, Büchner B and Woodward P M 2013 *J. Am. Chem. Soc.* **135** 18824
[18] Paul A K, Jansen M, Yan B, Felser C, Reehuis M and Abdala P M 2013 *Inorg. Chem.* **52** 6713
[19] Kobayashi K I, Kimura T, Tomioka Y, Sawada H and Terakura K 1999 *Phys. Rev. B* **59** 11159
[20] Vasilév A N and Volkova O S 2007 *Low Temp. Phys.* **33** 895
[21] Shimakawa Y, Shiraki H and Saito T 2008 *J. Phys. Soc. Jpn.* **77** 113702
[22] Ramirez A P, Subramanianb M A, Gardel M, Blumberg G, Li D, Vogtc T and Shapiro S M 2000 *Solid State Commun.* **115** 217
[23] Homes C C, Vogt T, Shapiro S M, Wakimoto S and Ramirez A P 2001 *Science* **293** 673
[24] Zeng Z, Greenblatt M, Subramanian M A and Croft M 1999 *Phys. Rev. Lett.* **82** 3164
[25] Alonso J A, Sánchez-Benítez J, Andrés A D, Marínez-Lope M J, Casais M T and Martínez J L 2003 *Appl. Phys. Lett.* **83** 2623
[26] Takata K, Yamada I, Azuma M, Takano M and Shimakawa Y 2007 *Phys. Rev. B* **76** 024429
[27] Mezzadri F, Calestani G, Calicchio M, Gilioli E, Bolzoni F, Cabassi R, Marezio M and Migliori A 2009 *Phys. Rev. B* **79** 100106(R)
[28] Long Y W, Saito T, Mizumaki M, Agui A and Shimakawa Y 2009 *J. Am. Chem. Soc.* **131** 16244
[29] Shimakawa Y 2008 *Inorg. Chem.* **47** 8562
[30] Long Y W, Hayashi N, Saito T, Azuma M, Muranaka S and Shimakawa Y 2009 *Nature* **458** 60
[31] Long Y W and Shimakawa Y 2010 *New J. Phys.* **12** 063029
[32] Chen W T, Long Y W, Saito T, Attfield J P and Shimakawa Y 2010 *J. Mater. Chem.* **20** 7282
[33] Long Y W, Kawakami T, Chen W T, Saito T, Watanuki T, Nakakura Y, Liu Q Q, Jin C Q and Shimakawa Y 2012 *Chem. Mater.* **24** 2235
[34] Long Y W, Saito T, Tohyama T, Oka K, Azuma M and Shimakawa Y 2009 *Inorg. Chem.* **48** 8489

[35] Yamada I, Etani H, Tsuchida K, Marukawa S, Hayashi N, Kawakami T, Mizumaki M, Ohgushi K, KusanoY, Kim J, Tsuji N, Takahashi R, Nishiyama N, Inoue T, Irifune T and Takano M 2013 *Inorg. Chem.* **52** 13751

[36] Wang X, Chai Y S, Zhou L, Cao H B, Cruz C, Yang J Y, Dai J H, Yin Y Y, Yuan Z, Zhang S J, Yu R Z, Azuma M, Shimakawa Y, Zhang H M, Dong S, Sun Y, Jin C Q and Long Y W 2015 *Phys. Rev. Lett.* **115** 087610

[37] Yang J Y, Zhou L, Cheng J G, Hu Z W, Kuo C, Pao C W, Jang L, Lee J F, Dai J H, Zhang S J, Feng S M, Kong P P, Yuan Z, Yuan J, Uwatoko Y, Liu T, Jin C Q and Long Y W 2015 *Inorg. Chem.* **54** 6433

[38] Liu T, Zhang Y J, Kanegawa S and Sato O 2010 *J. Am. Soc. Chem.* **132** 8250

[39] Koumousi E S, Jeon I R, Gao Q, Dechambenoit P, Woodruff D N, Merzeau P, Buisson L, Jia X, Li D, Volatron F, Mathoni'ere C and Clérac R 2014 *J. Am. Soc. Chem.* **136** 15461

[40] Cafun J D, Lejeune J, Baudelet F, Dumas P, Itié J P and Bleuzen A 2012 *Angew. Chem. Int. Ed.* **51** 9146

[41] Li X, Cui X H, Liu X W, Jin M Z, Xiao L Z and Zhao M Y 1991 *Hyperfine Interact.* **69** 851

[42] Blaauw C and Woude F 1973 *J. Phys. C: Solid State Phys.* **6** 1422

[43] Kawasaki S, Takano M and Takeda Y 1996 *J. Solid State Chem.* **121** 174

[44] Takano M, Nakanishi N, Takeda Y, Naka S and Takada T 1977 *Mater. Res. Bull.* **12** 923

[45] Etani H, Yamada I, Ohgushi K, Hayashi N, KusanoY, Mizumaki M, Kim J, Tsuji N, Takahashi R, Nishiyama N, Inoue T, Irifune T and Takano M 2013 *J. Am. Chem. Soc.* **135** 6100

[46] Rezaei N, Hansmann P, Bahramy M S and Arita R 2014 *Phys. Rev. B* **89** 125125

[47] Schmid H 1994 *Ferroelectrics* **162** 317

[48] Wang J, Neaton J B, Zheng H, Nagarajan V, Ogale S B, Liu B, Viehland D, Vaithyanathan V, Schlom D G, Waghmare U V, Spaldin N A, Rabe K M, Wuttig M and Ramesh R 2003 *Science* **299** 1719

[49] Kimura T, Goto T, Shintani H, Ishizaka K, Arima T and Tokura Y 2003 *Nature* **426** 55

[50] Spaldin N A and Fiebig M 2005 *Science* **309** 391

[51] Eerenstein W, Mathur N D and Scott J F 2006 *Nature* **442** 759

[52] Cheong S W and Mostovoy M 2007 *Nat. Mater.* **6** 13

[53] Ramesh R and Spaldin N A 2007 *Nat. Mater.* **6** 21

[54] Wang K F, Liu J M and Ren Z F 2009 *Adv. Phys.* **58** 321

[55] Tokura Y, Seki S and Nagaosa N 2014 *Rep. Prog. Phys.* **77** 076501

[56] Scott J F 2013 *NPG Asia Mater.* **5** e72

[57] Ma J, Hu J M, Li Z and Nan C W 2011 *Adv. Mater.* **23** 1062

[58] Van Aken B, Palstra T T M, Filippetti A and Spaldin N A 2004 *Nat. Mater.* **3** 164

[59] Ikeda N, Ohsumi H, Ohwada K, Ishii K, Inami T, Kakurai K, Murakami Y, Yoshii K, Mori S, Horibe Y and Kitô H 2005 *Nature* **436** 1136

[60] Chapon L C, Radaelli P G, Blake G R, Park S and Cheong S W 2006 *Phys. Rev. Lett.* **96** 097601

[61] Goto T, Kimura T, Lawes G, Ramirez A P and Tokura Y 2004 *Phys. Rev. Lett.* **92** 257201

[62] Kimura T, Lawes G and Ramirez A P 2005 *Phys. Rev. Lett.* **94** 137201

[63] Katsura H, Nagaosa N and Balatsky V 2005 *Phys. Rev. Lett.* **95** 057205

[64] Sergienko I A and Dagotto E 2006 *Phys. Rev. B* **73** 094434

[65] Sergienko I A, Şen C and Dagotto E 2006 *Phys. Rev. Lett.* **97** 227204

[66] Arima T 2007 *J. Phys. Soc. Jpn.* **76** 073702

[67] Mostovoy M 2006 *Phys. Rev. Lett.* **96** 067601

[68] Prodi A, Gilioli E, Gauzzi A, Licci F, Marezio M, Bolzoni F, Huang Q, Santoro A and Lynn J W 2004 *Nat. Mater.* **3** 48

[69] Johnson R D, Chapon L C, Khalyavin D D, Manuel P, Radaelli P G and Martin C 2012 *Phys. Rev. Lett.* **108** 067201

[70] Zhang G, Dong S, Yan Z, Guo Y, Zhang Q, Yunoki S, Dagotto E and Liu J M 2011 *Phys. Rev. B* **84** 174413

[71] N. Mufti, Nugroho A A, Blake G R and Palstra T T M 2010 *J. Phys.: Condens. Matter* **22** 075902

[72] King-Smith R D and Vanderbilt D 1993 *Phys. Rev. B* **47** 1651

[73] Bokov A A and Ye Z G 2006 *J. Mater. Sci.* **41** 31

[74] Lee J H, Jeong Y K, Park J H, Oak M A, Jang H M, Son J Y and Scott J F 2011 *Phys. Rev. Lett.* **107** 117201

[75] Johnson R D, Terada N and Radaelli P G 2012 *Phys. Rev. Lett.* **108** 219701

[76] Kuo C Y, Drees Y, Fernández-Díaz M T, Zhao L, Vasylechko L, Sheptyakov D, Bell A M T, Pi T W, Lin H J, Wu M K, Pellegrin E, Valvidares S M, Li Z W, Adler P, Todorava A, Küchler R, Steppke A, Tjeng L H, Hu Z and Komared A C 2014 *Phys. Rev. Lett.* **113** 217203

[77] Johnson R D, Cao K, Giustino F and Radaelli P G 2014 *Phys. Rev. B* **90** 045129

[78] Iyama A and Kimura T 2013 *Phys. Rev. B* **87** 180408(R)

[79] Scott J F 2008 *J. Phys.: Condens. Matter* **20** 021001

[80] Okazaki K and Maiwa H 1992 *Jpn. J. Appl. Phys.* **31** 3113

[81] Ramesha K, Llobet A, Proffen Th, Serrao C R and Rao C N R 2007 *J. Phys.: Condens. Matter* **19** 102202

[82] Amrani M, Zaghrioui M, Phuoc V, Gervais F and Massa N E 2014 *J. Magn. Magn. Mater.* **361** 1

[83] Kolev N, Bontchev R P, Jacobson A J, Popov V N, Hadjiev V G, Litvinchuk A P and Iliev M N 2002 *Phys. Rev. B* **66** 132102